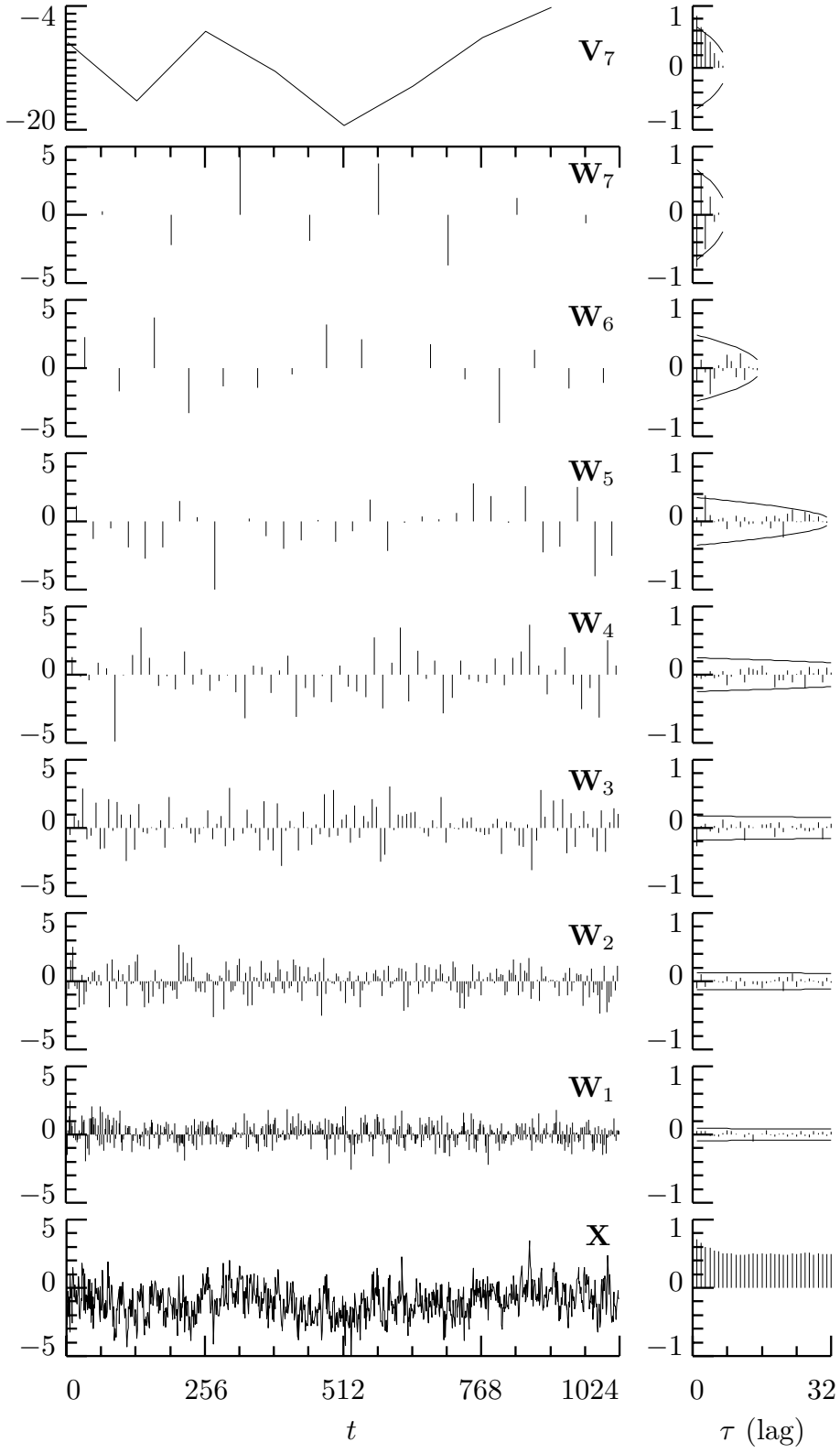

Figure 342. LA(8) DWT coefficients for simulated FD(0.4) time series and sample ACSs.

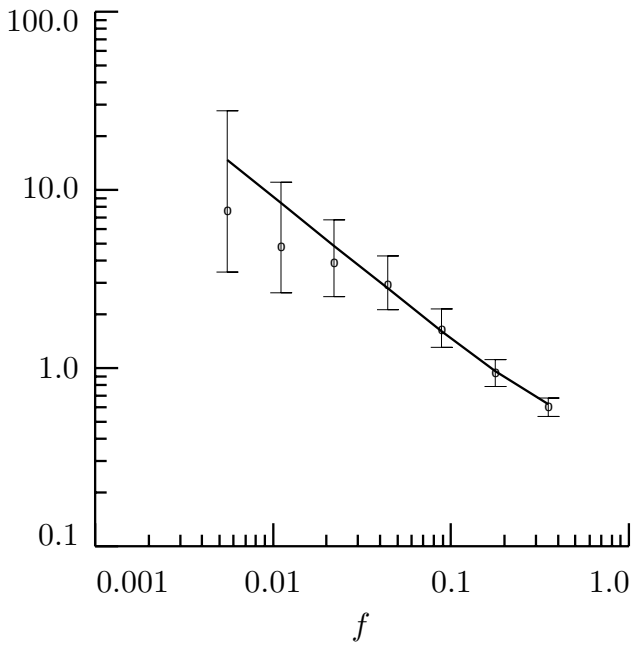

Figure 344. Sample variances of LA(8) wavelet coefficients from Figure 342 for – from right to left – levels $j = 1, \ldots, 7$ (circles) along with true FD(0.4) SDF evaluated at the center frequency $1/2^{j+\frac{1}{2}}$ of the octave bands $[\frac{1}{2^{j+1}}, \frac{1}{2^j}]$ (thick curve).

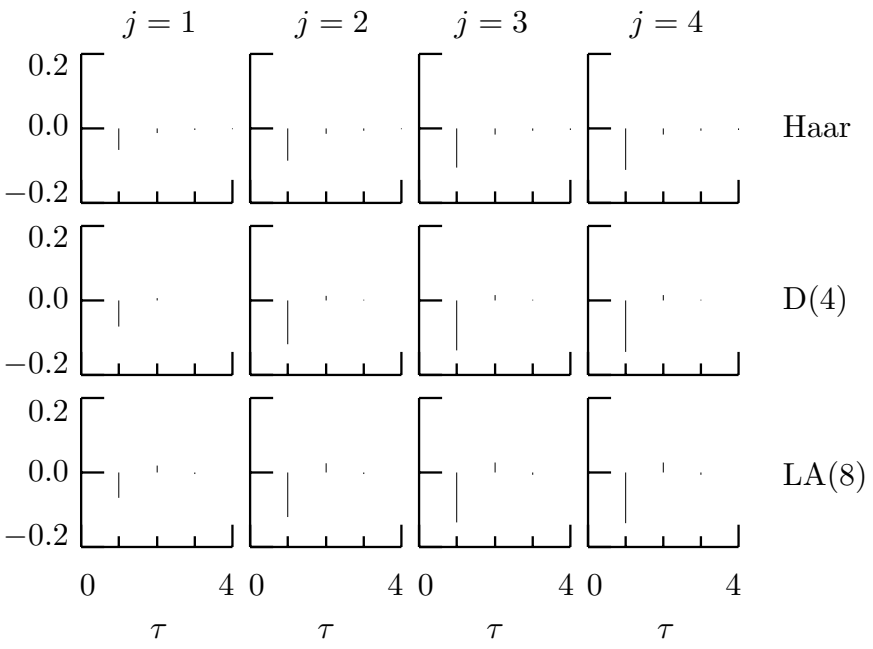

Figure 346a. ACSs at $\tau = 1, \ldots, 4$ for Haar, D(4) and LA(8) wavelet coefficients $W_{j,t}$, $j = 1, \ldots, 4$, of an FD(0.4) process. The ACS values are plotted as deviations from zero (some are not visible because they are so close to zero).

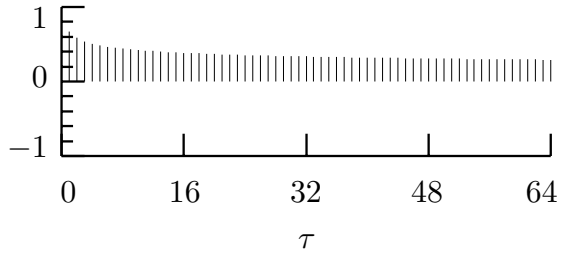

Figure 346b. ACS for FD process with $\delta = 0.4$ out to lag $\tau = 64$.

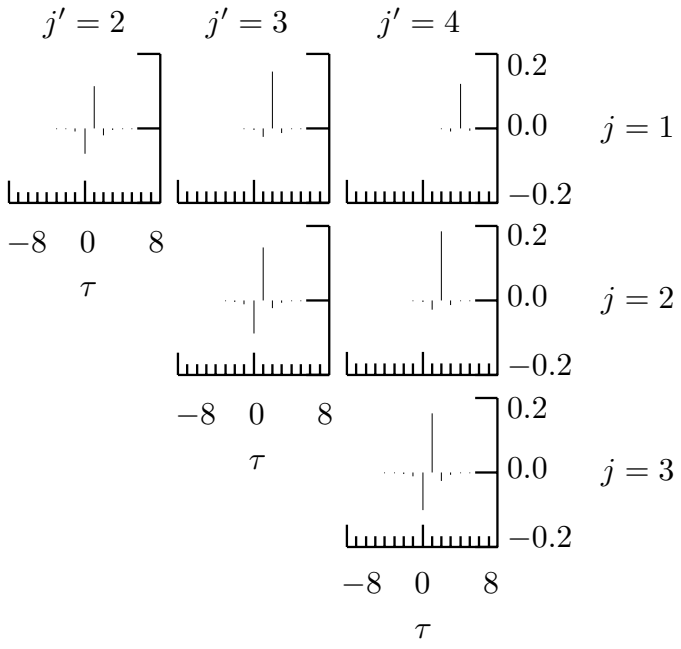

Figure 347a. Correlation between the Haar wavelet coefficients $W_{j,t}$ and $W_{j',t'}$ formed from an FD(0.4) process and for levels satisfying $1 \leq j < j' \leq 4$. By setting $t = 2^{|j'-j|-1}$ and $t' = t + \tau$ with $\tau = -8, \ldots, 8$, we capture two coefficients exhibiting the maximum absolute correlation over all possible combinations of t and t'.

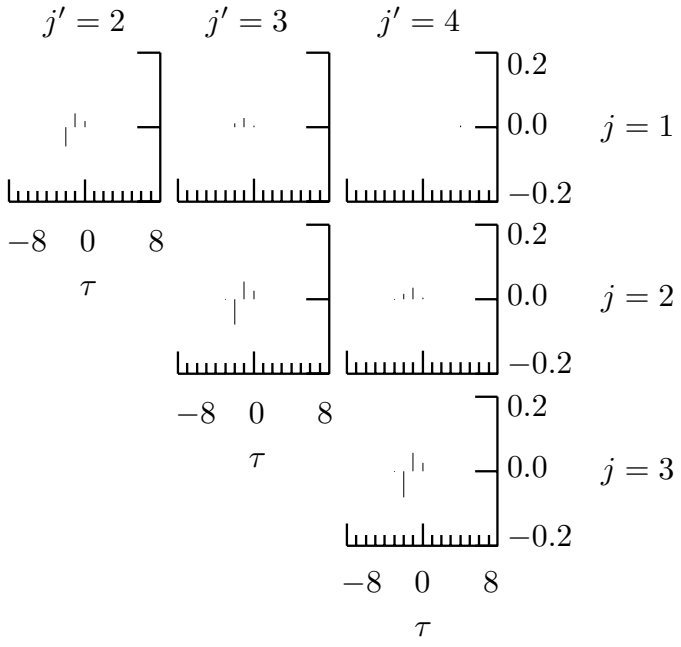

Figure 347b. As in Figure 347a, but now using the LA(8) DWT and with t set as per Equation (346).

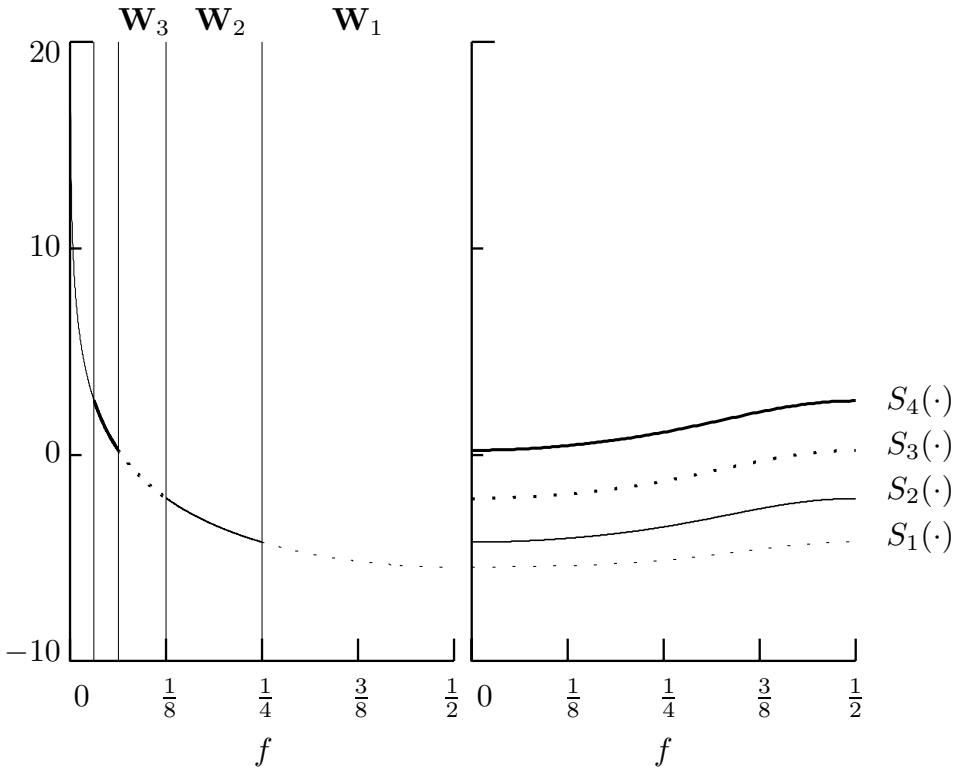

Figure 349. SDFs for an FD(0.4) process (left-hand plot) and for nonboundary LA(8) wavelet coefficients in $\mathbf{W}_1$, $\mathbf{W}_2$, $\mathbf{W}_3$ and $\mathbf{W}_4$ (right-hand). The vertical axis is in units of decibels (i.e., we plot $\log_{10}(S_X(f))$ versus f). The vertical lines in the left-hand plot denote the nominal pass-bands for the four $\mathbf{W}_j$.

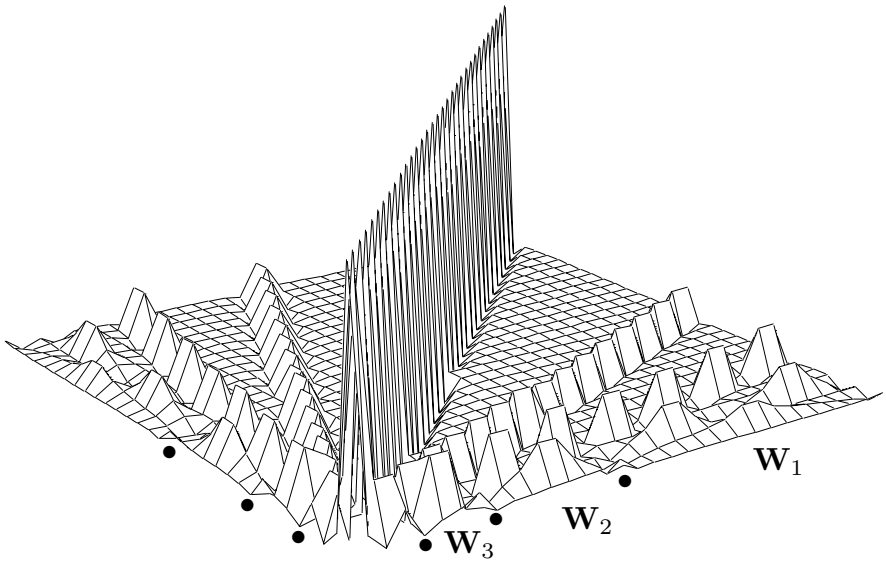

Figure 350. Correlation matrix of Haar wavelet coefficients for a portion of length $N = 32$ from an FD process with $\delta = 0.4$.

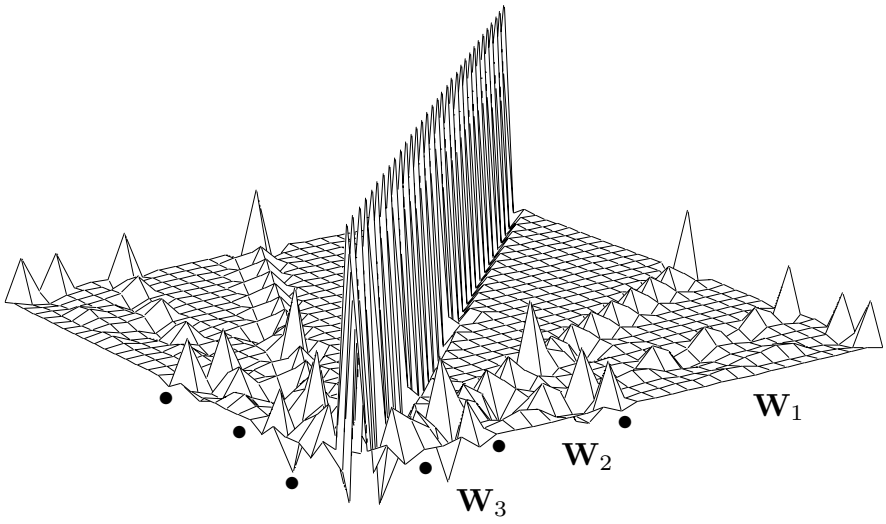

Figure 351a. As in Figure 350, but now using the D(4) DWT.

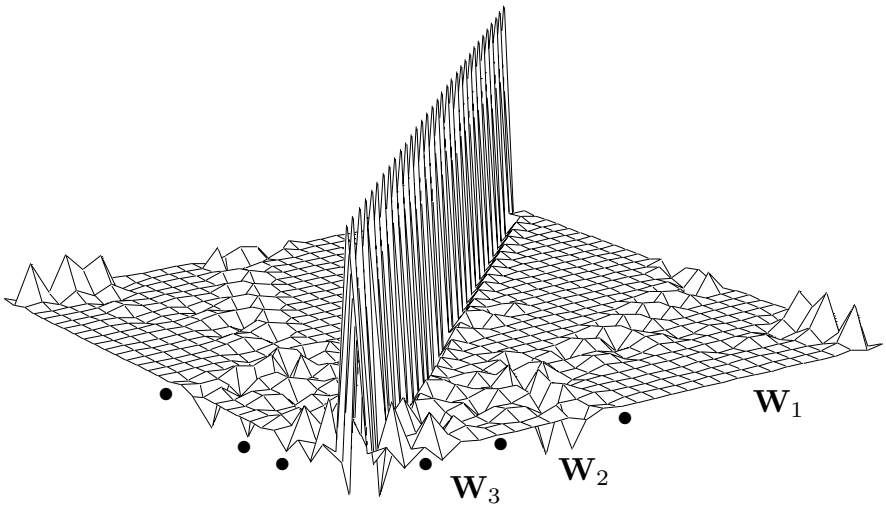

Figure 351b. As in Figure 350, but now using the LA(8) DWT.

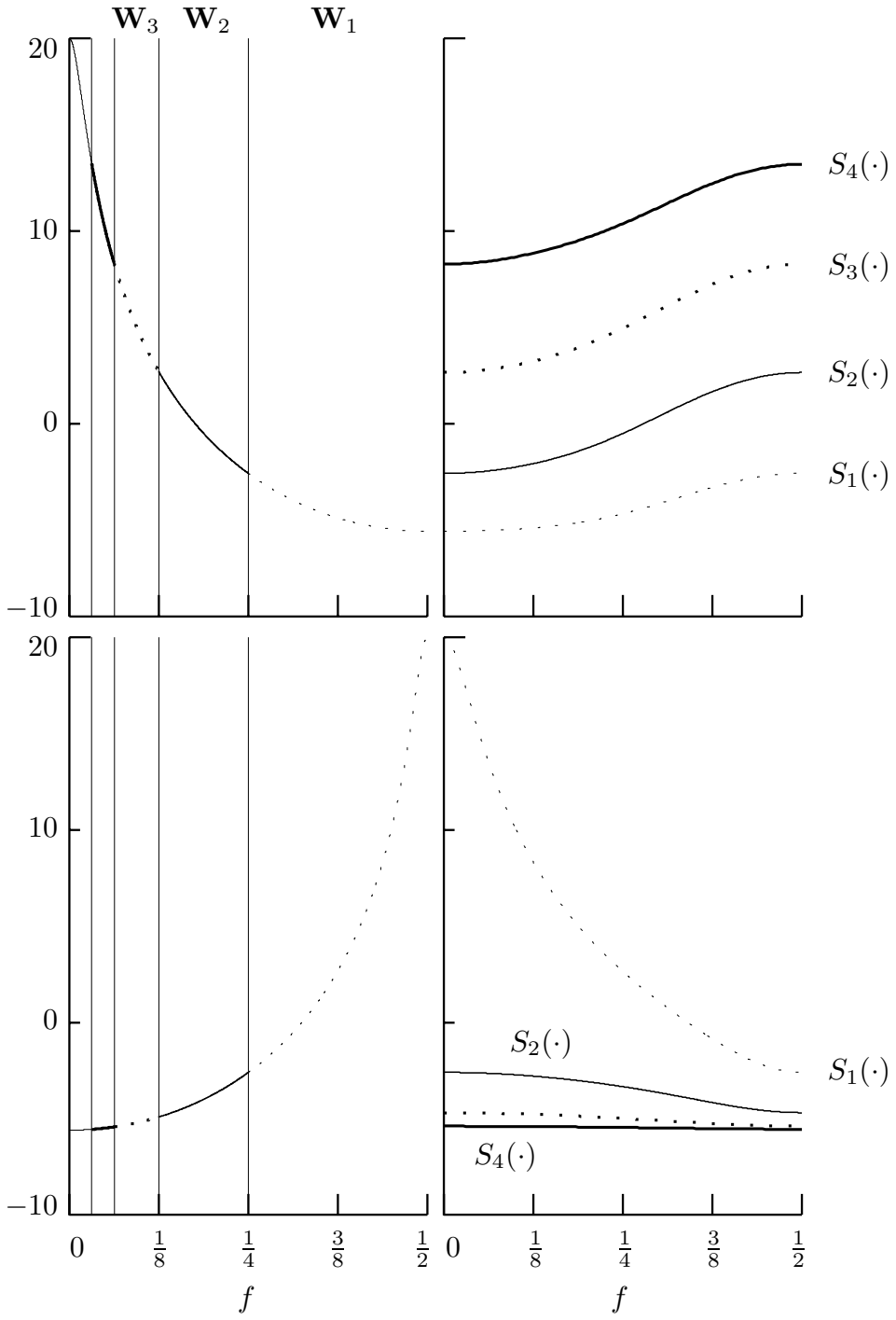

Figure 352. SDFs for AR(1) processes with $\phi = 0.9$ (top left-hand plot) and -0.9 (bottom left-hand) and for corresponding nonboundary LA(8) wavelet coefficients in $\mathbf{W}_1$ to $\mathbf{W}_4$ (right-hand plots). The vertical axes are in decibels, and the vertical lines in the left-hand plots delineate the nominal pass-bands for the four $\mathbf{W}_j$.

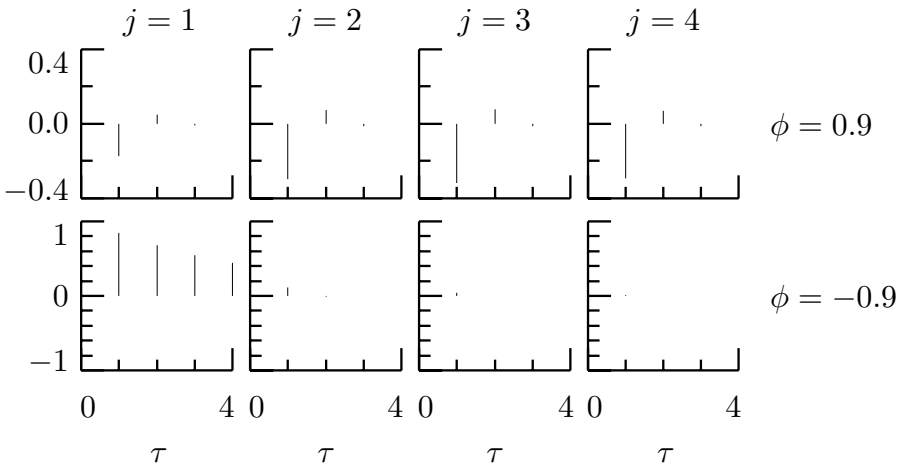

Figure 353. ACSs at $\tau = 1, \ldots, 4$ for LA(8) wavelet coefficients $W_{j,t}$, $j = 1, \ldots, 4$, of an AR(1) process with $\phi = 0.9$ and -0.9 (top and bottom rows, respectively).

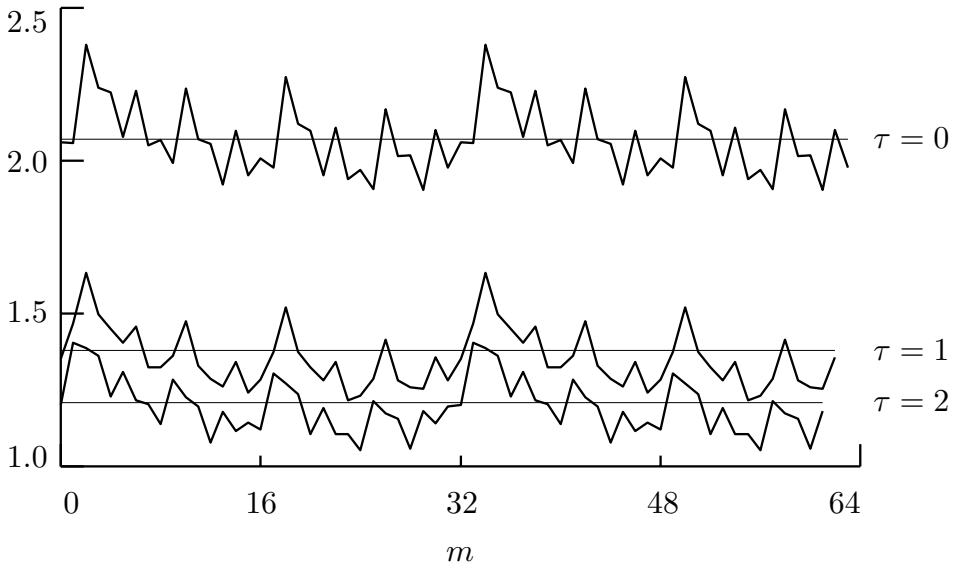

Figure 356. Diagonal elements $\Sigma_{\mathbf{Y},m,m+\tau}$ and $\Sigma_{\mathbf{X},m,m+\tau}$, $m = 0, \ldots, N-1-\tau$, of the covariance matrices $\Sigma_{\mathbf{Y}}$ and $\Sigma_{\mathbf{X}}$ (thick jagged curves and thin horizontal lines, respectively) for sample size $N = 64$ from an FD(0.4) process with $\sigma_\varepsilon^2 = 1$ and with $\Sigma_{\mathbf{Y}}$ constructed using an LA(8) DWT. Three diagonals are plotted for each covariance matrix, namely, the main diagonal ($\tau = 0$) and the first two off-diagonals ($\tau = 1$ and 2). Whereas $\Sigma_{\mathbf{X}}$ exhibits the Toeplitz structure required for a stationary process, its approximation $\Sigma_{\mathbf{Y}}$ does not.

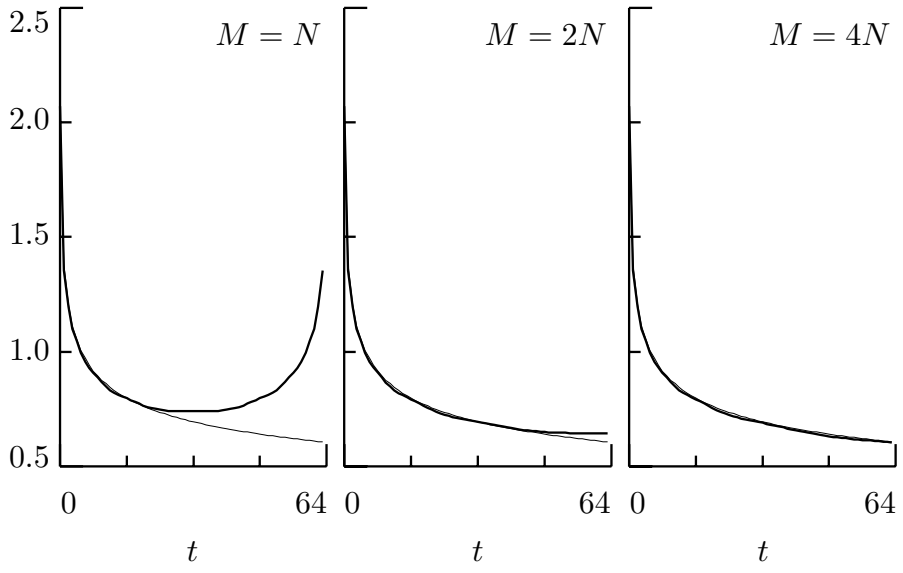

Figure 357. True ACVS (thin curves) and wavelet-based approximate ACVSs (thick) for an FD(0.4) process. The approximating ACVSs are based on an LA(8) DWT in which we generate a series of length M and then extract a series of length $N = 64$. As M goes from N to $4N$, the approximate ACVS gets closer to the true ACVS.

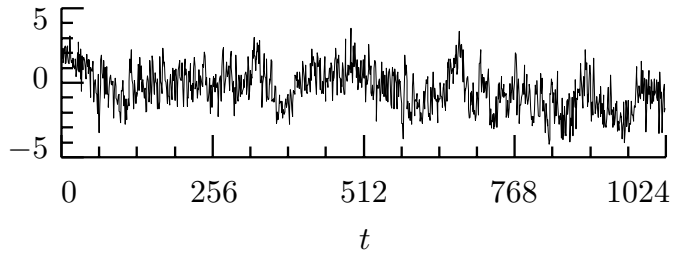

Figure 358. LA(8) wavelet-based simulation of a series of length $N = 1024$ from an FD process with zero mean and with parameters $\delta = 0.4$ and $\sigma_\varepsilon^2 = 1.0$.

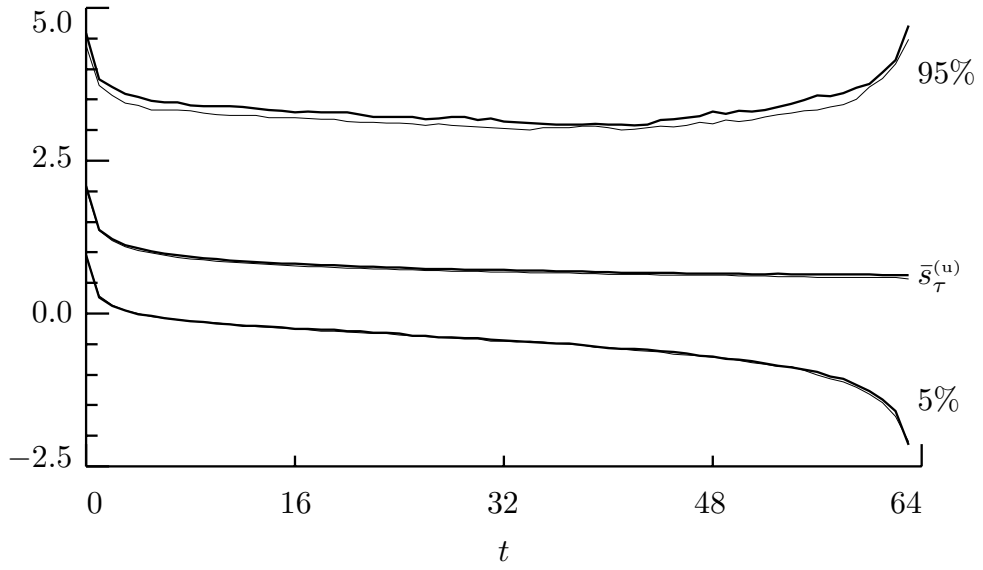

Figure 359. Estimated ACVSs averaged over 10 000 realizations generated via the Davies–Harte method (thin curve, middle of the plot) and the LA(8) wavelet-based method (thick curve) for an FD(0.4) process. The corresponding lower and upper pairs of curves indicate the 5% and 95% percentage points of the empirical distribution of the 10 000 simulations.

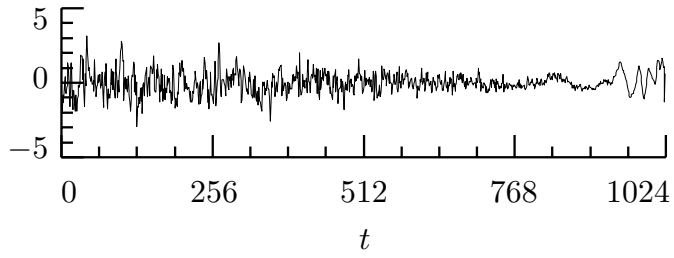

Figure 360. LA(8) wavelet-based simulation of a series of length $N = 1024$ from process with time varying statistical properties.

		MLE			
δ		Haar	D(4)	LA(8)	exact
0.25	mean	0.2184	0.2293	0.2328	0.2374
	bias	−0.0316	−0.0207	−0.0172	−0.0126
	SD	0.0713	0.0705	0.0710	0.0673
	RMSE	0.0780	0.0735	0.0731	0.0685
0.4	mean	0.3614	0.3727	0.3768	0.3797
	bias	−0.0386	−0.0273	−0.0232	−0.0203
	SD	0.0675	0.0652	0.0640	0.0604
	RMSE	0.0778	0.0707	0.0681	0.0637

Table 363. Sample mean, bias, standard deviation and root mean square error of 1024 wavelet-based approximate MLEs $\tilde{\delta}^{(s)}$ of the parameter δ based on the likelihood function of Equation (362a) using Haar, D(4) and LA(8) wavelet filters. All 1024 time series were of length $N = 128$ and were simulated using the Davies–Harte method. Corresponding statistics for exact MLEs $\hat{\delta}$ are given in the final column.

		MLE			
δ		Haar	D(4)	LA(8)	exact
0.25	mean	0.2256	0.2363	0.2402	0.2443
	bias	−0.0244	−0.0137	−0.0098	−0.0057
	SD	0.0505	0.0495	0.0502	0.0479
	RMSE	0.0561	0.0514	0.0511	0.0483
0.4	mean	0.3710	0.3832	0.3886	0.3900
	bias	−0.0290	−0.0168	−0.0114	−0.0100
	SD	0.0488	0.0478	0.0465	0.0437
	RMSE	0.0567	0.0506	0.0479	0.0448

Table 364. As in Table 363, but now with $N = 256$.

		MLE			
δ		Haar	D(4)	LA(8)	exact
0.25	mean	0.2058	0.2182	0.2227	0.2274
	bias	−0.0442	−0.0318	−0.0273	−0.0226
	SD	0.0559	0.0551	0.0557	0.0528
	RMSE	0.0712	0.0636	0.0620	0.0575
0.4	mean	0.3449	0.3602	0.3672	0.3687
	bias	−0.0551	−0.0398	−0.0328	−0.0313
	SD	0.0550	0.0538	0.0525	0.0494
	RMSE	0.0778	0.0669	0.0619	0.0585

Table 366. As in Table 364, but now with the process mean assumed unknown and hence estimated using the sample mean $\overline{X}$.

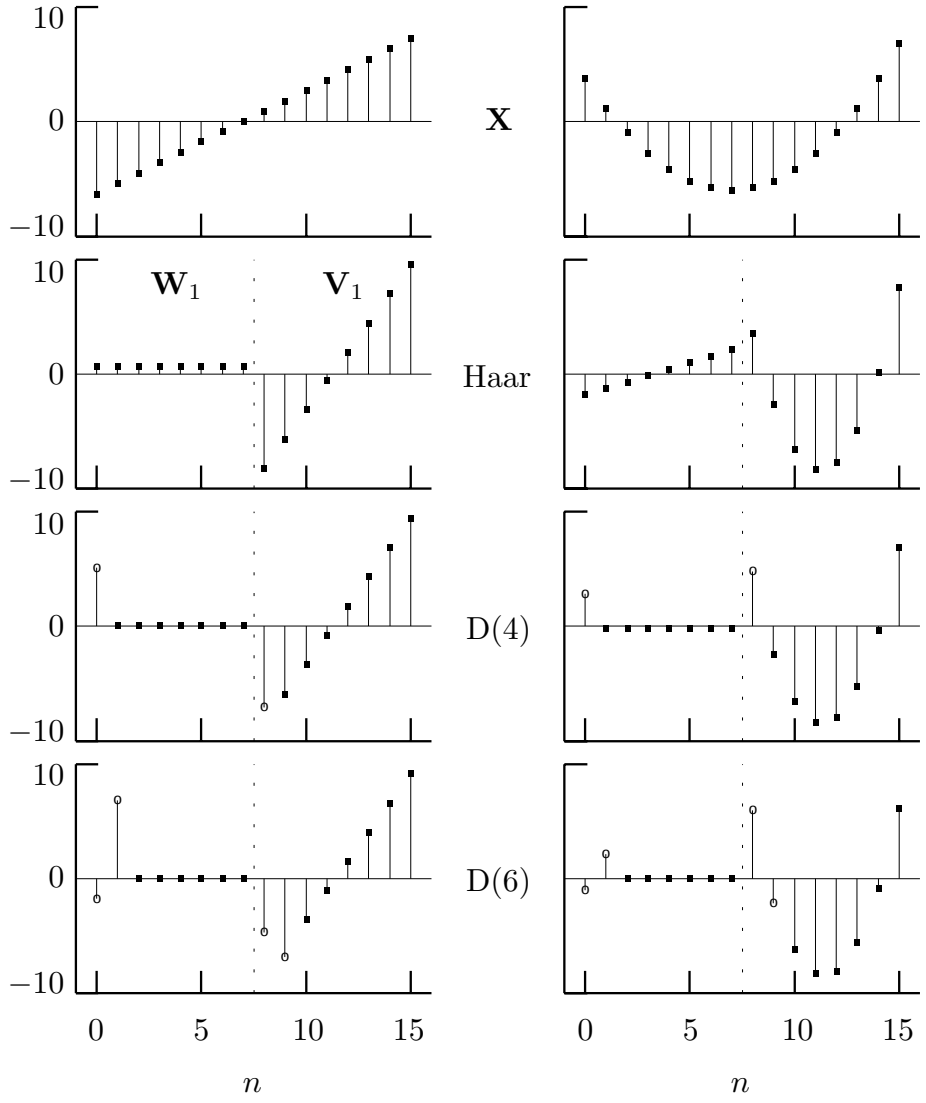

Figure 369. Linear and quadratic trends $\mathbf{T}$ (top plots), below which are shown their partial DWT coefficients $\mathbf{W} = [\mathbf{W}_1^T, \mathbf{V}_1^T]^T$ based on the Haar, D(4) and D(6) wavelet filters (second to fourth rows, respectively). The vertical dotted lines delineate the subvectors $\mathbf{W}_1$ and $\mathbf{V}_1$. Boundary wavelet and scaling coefficients are indicated by circles (there are none for the Haar; one each in $\mathbf{W}_1$ and $\mathbf{V}_1$ for the D(4); and two in each of the subvectors for the D(6)). Because the Haar wavelet does not reduce either linear or quadratic polynomials to zero, its wavelet coefficients are all nonzero; on the other hand, the D(6) wavelet reduces both polynomials to zero, so its six nonboundary wavelet coefficients are zero in both $\mathbf{W}_1$. The D(4) wavelet can handle a linear polynomial, but not a quadratic, which is why its seven nonboundary wavelet coefficients are zero for the former and nonzero for the latter. (For the record, the linear and quadratic trends are defined by $T_t = 0.9 \cdot (t - 7)$ and $T_t = 0.2 \cdot (t - 7)^2 - 6$. This illustration is due to W. Constantine, MathSoft, Seattle.)

		MLE			
δ		Haar	D(4)	LA(8)	exact
0.4	mean	0.3670	0.3762	0.3792	0.3900
	bias	−0.0330	−0.0238	−0.0208	−0.0100
	SD	0.0588	0.0732	0.0943	0.0437
	RMSE	0.0674	0.0769	0.0966	0.0448
	σ_δ	0.0530	0.0673	0.0869	
0.75	mean	0.7230	0.7277	0.7346	0.7677
	bias	−0.0270	−0.0223	−0.0154	0.0177
	SD	0.0783	0.0878	0.0863	0.0272
	RMSE	0.0829	0.0906	0.0877	0.0325
	σ_δ	0.0526	0.0665	0.0857	

Table 372. As in Table 364, but now using the likelihood function of Equation (371a) to define the wavelet-based approximate MLE $\tilde{\delta}^{(\mathrm{s/ns})}$ for δ (the $\delta = 0.4$ results for the exact MLE in the final column are replicated from Table 364). The nature of the term σ_δ is explained in the text.

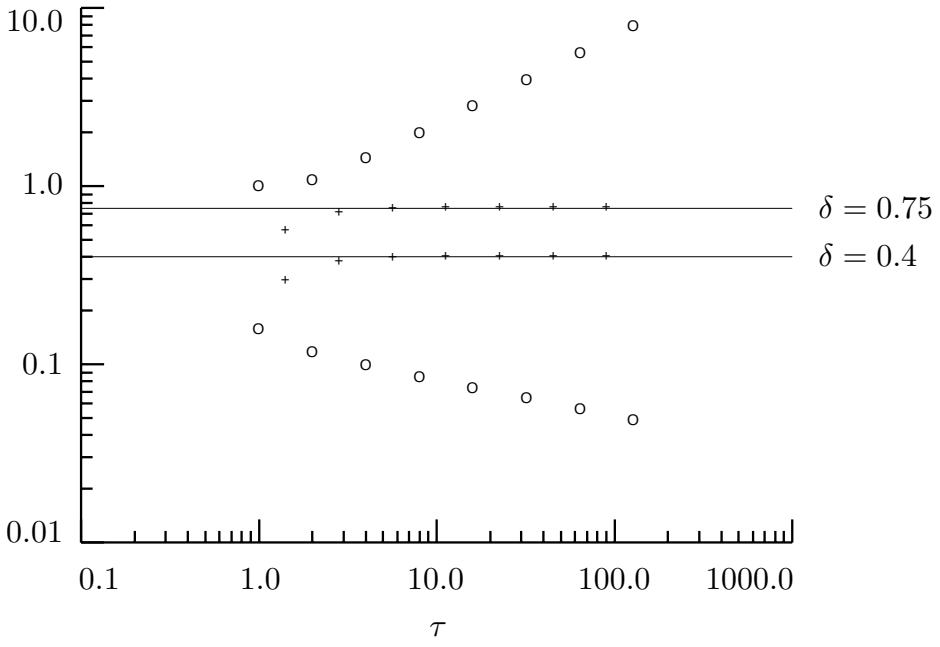

Figure 375. Approximations $C_j/2^j$ (computed from Equation (343b) via numerical integration) to wavelet variances $\nu_X^2(\tau_j)$ versus scales τ_j, $j = 1, \ldots, 8$, for FD processes with $\delta = 0.4$ (lower circles) and 0.75 (upper). See the text for an explanation of the portion of the plot between these sets of circles.

		WLSE			MLE
δ		Haar	D(4)	LA(8)	exact
0.4	mean	0.3925	0.4006	0.4044	0.3900
	bias	−0.0075	0.0006	0.0044	−0.0100
	SD	0.0715	0.0886	0.1185	0.0437
	RMSE	0.0719	0.0886	0.1186	0.0448
0.75	mean	0.7398	0.7443	0.7435	0.7677
	bias	−0.0102	−0.0057	−0.0065	0.0177
	SD	0.0779	0.0877	0.1196	0.0272
	RMSE	0.0786	0.0879	0.1198	0.0325
	$\sqrt{\text{var}\,\{\hat{\beta}^{(\text{wls})}\}}$	0.0891	0.1145	0.1552	

Table 377. As in Table 372, but now using the wavelet-based WLSE $\hat{\delta}^{(\text{wls})}$ (the final column is replicated from Table 372). The WLSEs are based on the unbiased MODWT estimators $\hat{\nu}^2_X(\tau_j)$ of the wavelet variance, which are presumed to have EDOFs $\eta_j = \max\{M_j/2^j, 1\}$. We set $J_1 = 2$ for all three wavelets. The results reported in the table are based on 1024 simulated time series of sample size $N = 256$.

		WLSE			MLE
δ		Haar	D(4)	LA(8)	exact
0.4	mean	0.3881	0.3994	0.4000	0.3900
	bias	−0.0119	−0.0006	−0.0000	−0.0100
	SD	0.0669	0.0700	0.0728	0.0437
	RMSE	0.0680	0.0700	0.0728	0.0448
0.75	mean	0.7278	0.7432	0.7442	0.7677
	bias	−0.0222	−0.0068	−0.0058	0.0177
	SD	0.0739	0.0718	0.0726	0.0272
	RMSE	0.0772	0.0721	0.0728	0.0325

Table 378. As in Table 377, but now using an WLSE $\tilde{\delta}^{(\mathrm{wls})}$ based upon a biased MODWT estimator of the wavelet variance along with reflection boundary conditions.

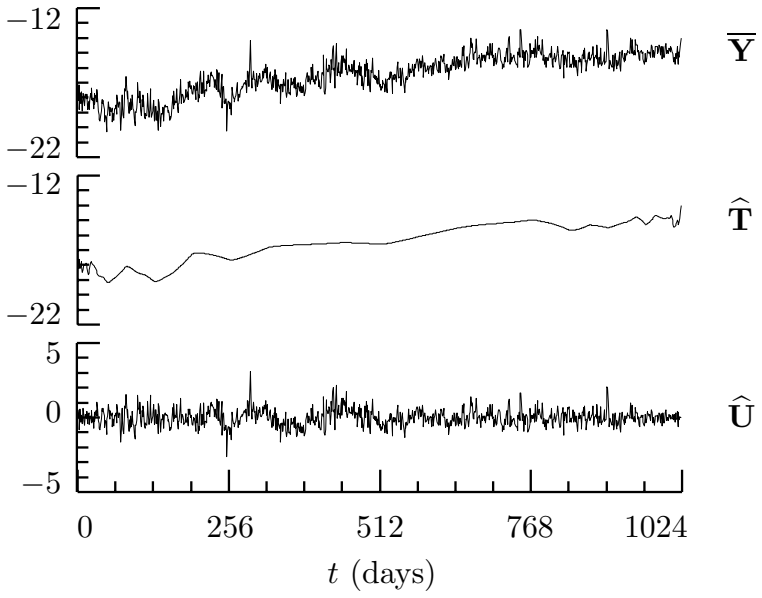

Figure 383. Wavelet-based decomposition of atomic clock fractional frequency deviates $\overline{\mathbf{Y}}$ into an estimated trend $\widehat{\mathbf{T}}$ and residuals $\widehat{\mathbf{U}}$ about the trend. Here we used an LA(8) partial DWT of level $J_0 = 7$. Note that $\widehat{\mathbf{T}}$ has much more structure than a low order polynomial and in fact resembles the output from a variable bandwidth smoother: it is quite smooth near the middle of the series, but then becomes rougher in appearance toward the end points.

	Haar	D(4)	LA(8)
$\tilde{\delta}^{(\mathrm{s/ns})}$	0.5031	0.3943	0.3921
$\sigma_{\tilde{\delta}^{(\mathrm{s/ns})}}$	0.0252	0.0282	0.0318
$\tilde{\sigma}_{\varepsilon}^2$	0.3057	0.2838	0.2740
$\hat{\delta}^{(\mathrm{wls})}$	0.4449	0.3812	0.3460
$\sqrt{\mathrm{var}\,\{\hat{\delta}^{(\mathrm{wls})}\}}$	0.0374	0.0418	0.0479
J_0	10	8	7

Table 384. Parameter estimation for the atomic fractional frequency deviates (see text for details).

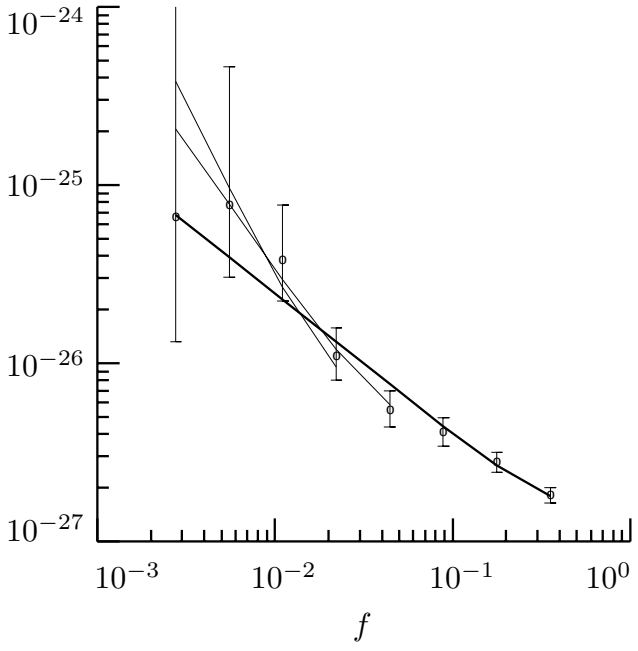

Figure 384. D(4) MODWT wavelet variance estimates for atomic clock fractional frequency deviates (re-expressed as spectral levels C_j), along with spectral levels deduced from MLEs of δ and σ_{ε}^2 (thick curve). The two shorter thin curves are discussed in the text.

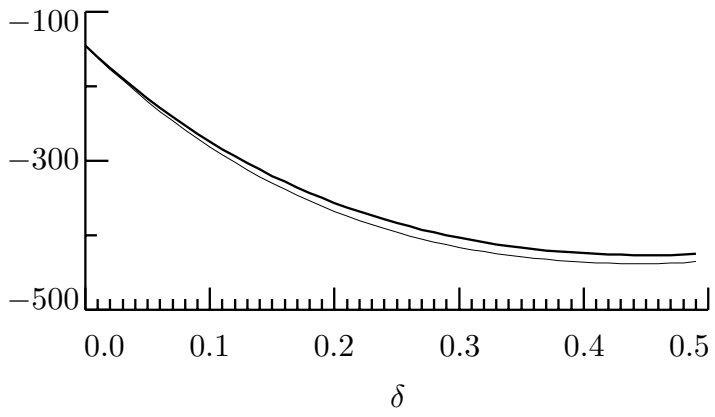

Figure 386. Reduced log likelihood functions for the FD parameter δ computed using the final 512 observations of the Nile River time series (see Figure 192). The thick curve is based on the LA(8) wavelet and attains its minimum at the estimate $\tilde{\delta}^{(\mathrm{s})} \doteq 0.4532$, while the thin curve is for the exact method and reaches its minimum at $\hat{\delta} \doteq 0.4452$.

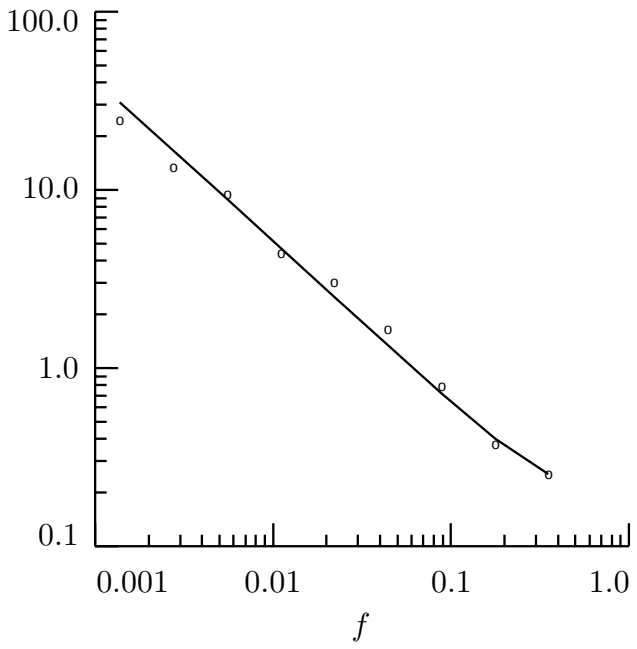

Figure 387. Variance of wavelet coefficients computed via LA(8) MLEs $\tilde{\delta}^{(s)}$ and $\tilde{\sigma}^2_{\varepsilon}(\tilde{\delta}^{(s)})$ (solid curve) as compared to sample variances of LA(8) wavelet coefficients (circles).

			critical levels		
τ_j	M'_j	D	10%	5%	1%
1 year	331	0.1559	0.0945	0.1051	0.1262
2 years	165	0.1754	0.1320	0.1469	0.1765
4 years	82	0.1000	0.1855	0.2068	0.2474
8 years	41	0.2313	0.2572	0.2864	0.3436

Table 387. Results of testing Nile River minima for homogeneity of variance using the Haar wavelet filter critical values determined by computer simulations (Whitcher *et al.*, 2000a).

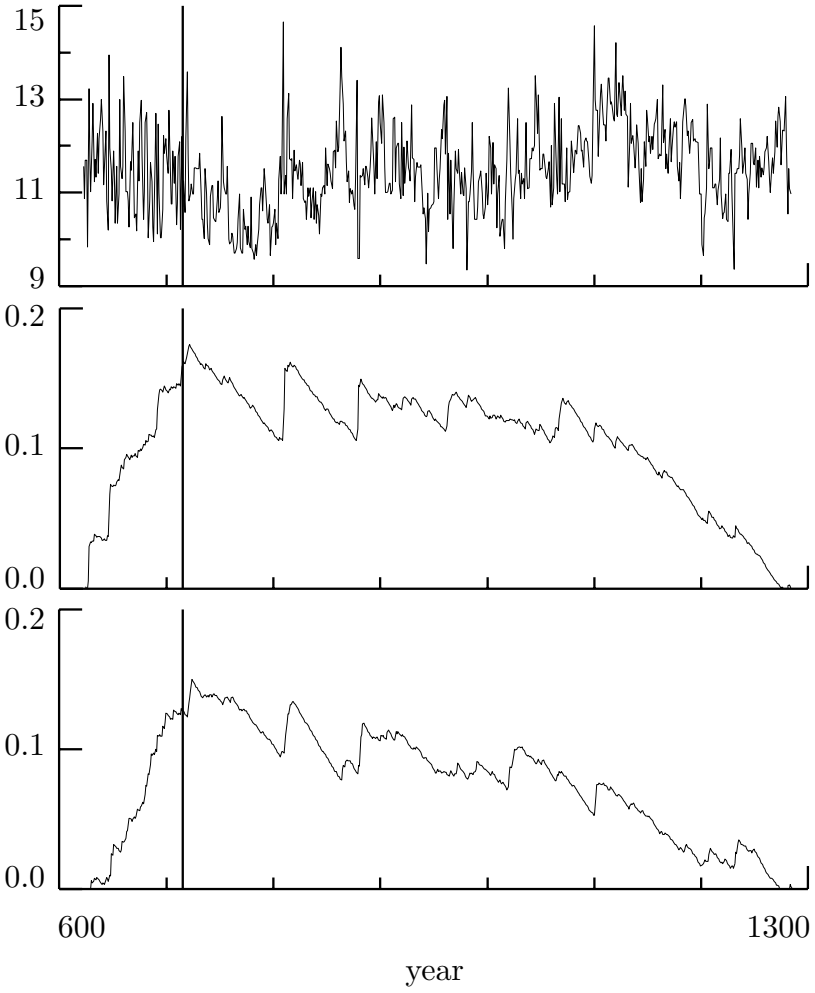

Figure 388. The Nile River minima (top plot) along with Δ_k^- versus k for scales τ_1 and τ_2 (middle and bottom plots, respectively). The thick vertical lines denote the year 715.